Revisiting the Distance, Environment, and Supernova Properties of SNR G57.2+0.8 that Hosts SGR 1935+2154

Zhou, P.; Zhou, X.; Chen, Y.; Wang, J.-S.; Vink, J.; Wang, Y.

DOI
10.3847/1538-4357/abc34a

Publication date
2020

Document Version
Final published version

Published in
Astrophysical Journal

The Astrophysical Journal, 905:99 (12pp), 2020 December 20 https://doi.org/10.3847/1538-4357/abc34a

Revisiting the Distance, Environment, and Supernova Properties of SNR G57.2+0.8 that Hosts SGR 1935+2154

Ping Zhou[1], Xin Zhou[2], Yang Chen[3,4], Jie-Shuang Wang[5], Jacco Vink[1,6,7], and Yuan Wang[8]
[1] Anton Pannekoek Institute for Astronomy, University of Amsterdam, Science Park 904, 1098 XH Amsterdam, The Netherlands; p.zhou@uva.nl
[2] Purple Mountain Observatory and Key Laboratory of Radio Astronomy, Chinese Academy of Sciences, 10 Yuanhua Road, Nanjing 210023, People's Republic of China; xinzhou@pmo.ac.cn
[3] School of Astronomy and Space Science, Nanjing University, 163 Xianlin Avenue, Nanjing 210023, People's Republic of China
[4] Key Laboratory of Modern Astronomy and Astrophysics, Nanjing University, Ministry of Education, Nanjing, People's Republic of China
[5] Tsung-Dao Lee Institute, Shanghai Jiao Tong University, Shanghai 200240, People's Republic of China
[6] GRAPPA, University of Amsterdam, Science Park 904, 1098 XH Amsterdam, The Netherlands
[7] SRON, Netherlands Institute for Space Research, Sorbonnelaan 2, 3584 CA Utrecht, The Netherlands
[8] Max Planck Institute for Astronomy, Königstuhl 17, D-69117 Heidelberg, Germany
Received 2020 May 7; revised 2020 October 4; accepted 2020 October 5; published 2020 December 17

Abstract

We have performed a multiwavelength study of supernova remnant (SNR) G57.2+0.8 and its environment. The SNR hosts the magnetar SGR 1935+2154, which emitted an extremely bright millisecond-duration radio burst on 2020 April 28. We used the ^{12}CO and ^{13}CO $J = 1$–0 data from the Milky Way Image Scroll Painting CO line survey to search for molecular gas associated with G57.2+0.8, in order to constrain the physical parameters (e.g., the distance) of the SNR and its magnetar. We report that SNR G57.2+0.8 is likely impacting the molecular clouds (MCs) at the local standard of rest (LSR) velocity $V_{\rm LSR} \sim 30$ km s^{-1} and excites a weak 1720 MHz OH maser with a peak flux density of 47 mJy beam^{-1}. The chance coincidence of a random OH spot falling in the SNR is $\leqslant$12%, and the OH–CO correspondence chance is 7% at the maser spot. This combines to give <1% false probability of the OH maser, suggesting a real maser detection. The LSR velocity of the MCs places the SNR and magnetar at a kinematic distance of 6.6 ± 0.7 kpc. The nondetection of thermal X-ray emission from the SNR and the relatively dense environment suggests G57.2+0.8 be an evolved SNR with an age $t \gtrsim 1.6 \times 10^4 (d/6.6\ {\rm kpc})$ yr. The explosion energy of G57.2+0.8 is lower than $2 \times 10^{51} (n_0/10\ {\rm cm^{-3}})^{1.16} (d/6.6\ {\rm kpc})^{3.16}$ erg, which is not very energetic even assuming a high ambient density $n_0 = 10\ {\rm cm^{-3}}$. This reinforces the opinion that magnetars do not necessarily result from very energetic supernova explosions.

Unified Astronomy Thesaurus concepts: Molecular clouds (1072); Supernova remnants (1667); Radio transient sources (2008); Magnetars (992); X-ray bursts (1814); Soft gamma-ray repeaters (1471)

1. Introduction

On 2020 April 28 at UTC 14:34:33 an extremely bright millisecond-duration radio burst was detected from the direction of SGR 1935+2154 by the Canadian Hydrogen Intensity Mapping Experiment (CHIME) in the 400–800 MHz band (The CHIME/FRB Collaboration et al. 2020). Simultaneously, the Survey for Transient Astronomical Radio Emission 2 (STARE2) was triggered by this burst, and its fluence in the 1.4 GHz band was found to be >1.5 MJy ms (Bochenek et al. 2020). The magnetar SGR 1935+2154 was previously detected in active states by the X-ray and γ-ray telescopes such as Swift, NICER, and Fermi-LAT (Barthelmy et al. 2020; Fletcher & Fermi GBM Team 2020; Palmer & BAT Team 2020; Younes et al. 2017). This radio burst was subsequently found to correspond to a hard X-ray burst, which was detected by INTEGRAL (Mereghetti et al. 2020), AGILE (Tavani et al. 2020), Insight-HXMT (Li et al. 2020), and Konus-Wind (Ridnaia et al. 2020). More specifically, Insight-HXMT detected a double-peaked hard X-ray counterpart from SGR 1935+2154 8.57 s ahead of the radio double-peaked bursts. This unambiguously established a relationship between the extraordinary fast radio burst (FRB)-like radio burst (Bochenek et al. 2020; The CHIME/FRB Collaboration et al. 2020) and the magnetar, given that there is no intrinsic delay between radio and X-ray bursts after a correction of the dispersion measure (DM; Li et al. 2020). While FRBs have been regarded as millisecond-duration radio transients from cosmological distances (see a recent review by Petroff et al. 2019), the new FRB or FRB-like burst from SGR 1935+2154 provides the first nearby, Galactic target for us to study in detail.

While many observational and theoretical studies have been underway for this particular burst event in our Galaxy, the current understanding of the host of SGR 1935+2154—supernova remnant (SNR) G57.2+0.8 (Sieber & Seiradakis 1984)—is still limited. The distance, age, and explosion properties are shared between the magnetar and SNR. Therefore, the study of G57.2+0.8 provides essential information for the magnetar and also its radio bursts. The association between G57.2+0.8 and SGR 1935+2154, located in its geometric center, was only proposed recently (Gaensler 2014), shortly after the discovery of SGR 1935+2154 (Cummmings et al. 2014). The small characteristic age of SGR 1935+2154 (3600 yr; Israel et al. 2016) also supports that its SNR should be visible.

There have been many disputes on the distance of SGR 1935+2154. Most of the distance measurements were targeted to SNR G57.2+0.8, but from the blackbody emission of SGR 1935+2154, Kozlova et al. (2016) estimated an upper limit of the distance to be <10.0 kpc. An assumed distance of 9 kpc was adopted for the magnetar SGR 1935+2154 by Israel et al. (2016) and Younes et al. (2017), who referred to the presumed distance of G57.2+0.8 from the empirical relation of radio surface-brightness–distance (Σ–D) for SNRs (Pavlovic et al. 2014), a method with a large intrinsic scatter. The distances of ~7 kpc and 14.3 kpc were proposed in different studies using

this relation (Park et al. 2013; Pavlovic et al. 2014). The lower limit of the distance (4.5 kpc) has been constrained from the H I absorption feature toward the SNR at the local standard of rest (LSR) velocity $V_{\rm LSR} \sim 40$ km s^{-1} (Kothes et al. 2018; Ranasinghe et al. 2018). Overall various estimates are obtained based on the H I absorption method, from a far distance of 11.7 ± 2.8 kpc (Surnis et al. 2016) to a closer distance of 4.5–9 kpc (Ranasinghe et al. 2018). Kothes et al. (2018) favored a distance of 12.5 ± 1.5 kpc, due to a morphological match between an H I cavity at $V_{\rm LSR} = -51$ to -44 km s^{-1} and the SNR. The distance inferred from the dispersion measure is ∼9 or 15 kpc, varying with electron distribution models (Kothes et al. 2018; Zhong et al. 2020).

Motivated by the uncertain distance and poorly known SNR properties of G57.2+0.8, and their potential utilization in the understanding of the radio burst occurring on 2020 April 28, we performed a molecular environment study of G57.2+0.8. We show here that the SNR is likely associated with a molecular cloud (MC), which helps to constrain the distance by comparing the LSR velocity with the Galactic rotation curve (e.g., Reid et al. 2014). We also revisited the multiwavelength data to constrain the SNR properties such as the SNR age and explosion energy, which are the shared properties for the magnetar SGR 1935+2154. Simultaneously with this paper, Mereghetti et al. (2020) reported an independent distance measurement (3.1–7.2 kpc) using the dust scattering X-ray halo around SGR 1935+2154, which covers our suggested value of 6.6 ± 0.7 kpc.

2. Data in the Multiwave bands

We obtained ^{12}CO $J = 1$–0 and ^{13}CO $J = 1$–0 data from the Milky Way Image Scroll Painting (MWISP)[9]–CO line survey project. The project is an unbiased high-sensitivity survey toward the Galactic plane using the Purple Mountain Observatory (PMO) Delingha 13.7 m millimeter-wavelength telescope with a 3×3 multibeam sideband separation superconducting receiver (Shan et al. 2012) as the front end and a fast Fourier transform spectrometer (1 GHz total bandwidth) as the back end. The half-power beamwidth was about 55″. The typical rms noise level is ∼0.5 K for ^{12}CO ($J = 1$–0) in a 0.17 km s^{-1} channel and ∼0.3 K for ^{13}CO($J = 1$–0) in a 0.16 km s^{-1} channel. A detailed description of the observation can be found in Zhou et al. (2016). All data were reduced using the GILDAS/CLASS package.

We retrieved the Very Large Array (VLA) radio continuum image at 1.4 GHz, the data cubes of 1720, 1667, 1665 and 1612 MHz OH lines, and H I data from the H I/OH/recombination line survey (THOR) project (Beuther et al. 2016; Wang et al. 2020). The combined THOR plus the VLA Galactic Plane Survey 1.4 GHz image provides a spatial resolution of 25″. The OH data cubes have an angular resolution of ∼12″ and a velocity resolution of 1.5 km s^{-1}. The LSR velocity range of data cube spans from −58.5–135 km s^{-1}. We also retrieved Spitzer 24 μm post-basic-calibrated data from the Spitzer archive. The mid-IR observation was performed as a 24 Micron Survey of the Inner Galactic Disk Program (PID: 20597; PI: S. Carey).

We revisited all the available XMM-Newton data of G57.2+0.8 to search for its extended X-ray emission. The archival Chandra observations were not used as they covered only a small fraction of the SNR. G57.2+0.8 was observed with XMM-Newton in five epochs during 2014 and 2015 (OBSIDs: 0722412801, 0722413001, 0748390801, 0764820101, and 0764820201, PIs: G. Israel or N. Schartel). After removing the high background periods from the events, the screened exposure time of pn, MOS1, and MOS2 are 53 ks, 93 ks, and 85 ks, respectively. The XMM-Newton data were reduced using the Science Analysis System software (SAS, version 16.7.0). Finally, we obtained the background-subtracted, vignetting-corrected, and adaptively smoothed image of G57.2+0.8, with all of the pn and MOS images combined.

[9] http://english.dlh.pmo.cas.cn/ic/

3. Results

3.1. Molecular Environment of G57.2+0.8

The overall ^{12}CO ($J = 1$–0) spectrum in the field of view (FOV) shows several velocity components, $V_{\rm LSR} = -10$–15 km s^{-1} and $V_{\rm LSR} = 15$–50 km s^{-1} (see the first panel in Figure 1). There is also faint CO emission at around $V_{\rm LSR} = -40$ km s^{-1}, but it is too weak to be discerned in the overall spectrum and the emission is found outside the SNR boundary (see Figure 13 in Appendix C). Figure 1 shows the distribution of ^{12}CO emission toward G57.2+0.8 from $V_{\rm LSR} = 4$ km s^{-1} to 50 km s^{-1}. The morphological overlap between the SNR and MCs has been found only in two velocity ranges, $V_{\rm LSR} = 6$–14 km s^{-1} and 30 km s^{-1}.

The strong and diffuse CO emission at $V_{\rm LSR} = 6$–14 km s^{-1} is probably from nearby MCs at ∼1 kpc. However, this velocity also corresponds to a far distance of ∼8 kpc according to the Galactic rotation curve (Reid et al. 2014). At ∼12 km s^{-1}, the ^{12}CO intensity map shows a weak gradient from the east to the west and some enhancement along the remnant eastern edge. The gradient and enhancement might explain the morphology of radio emission of G57.2+0.8 in principle. However, no physical evidence (e.g., line broadening, heating, 1720 MHz OH masers; Jiang et al. 2010; Chen et al. 2014) of SNR–MC interaction is found in the velocity range of 6–14 km s^{-1}, in which multiple velocity components are crowding.

At $V_{\rm LSR} \sim 30$ km s^{-1}, there are two prominent molecular features near G57.2+0.8, a molecular bar connecting to the radio shell and an arc-like structure in the SNR south. The ^{12}CO and ^{13}CO spectra from the arc-like structure are presented in Figure 2 and the extraction region is shown in the upper panel of Figure 3. The ^{12}CO line profile contains a narrow component at $V_{\rm LSR} \sim 30$ km s^{-1} and a broad wing in the range of 30–45 km s^{-1}, while a weak ^{13}CO emission is only seen at the narrow component. We fitted the two ^{12}CO components with two Gaussian lines, providing FWHM line widths of 2.6 ± 0.1 km s^{-1} and 12.1 ± 1.3 km s^{-1} for the narrow and broad lines, respectively. For the broad ^{12}CO component, the line centroid and intensity are 35.5 ± 0.6 km s^{-1} and 0.31 ± 0.02 K, respectively. For the narrow ^{12}CO component, the line centroid and intensity are 29.12 ± 0.03 km s^{-1} and 1.94 ± 0.06 K, respectively. Using more Gaussian components does not significantly improve the fitting, as there is no extra component notable in the residuals.

The existence of a broad ^{12}CO component with a width of $dV \sim 12$ km s^{-1} indicates an interaction between the remnant and the MC, as a line broader than typical molecular lines requires external perturbation. According to Larson's third law (Larson 1981), the MC velocity dispersion σ is correlated to the cloud size L, $\sigma\,({\rm km\ s^{-1}}) = 1.1L({\rm\ pc})^{0.38}$. This suggests that the typical molecular line width $dV = 2.355\sigma$ is within a few

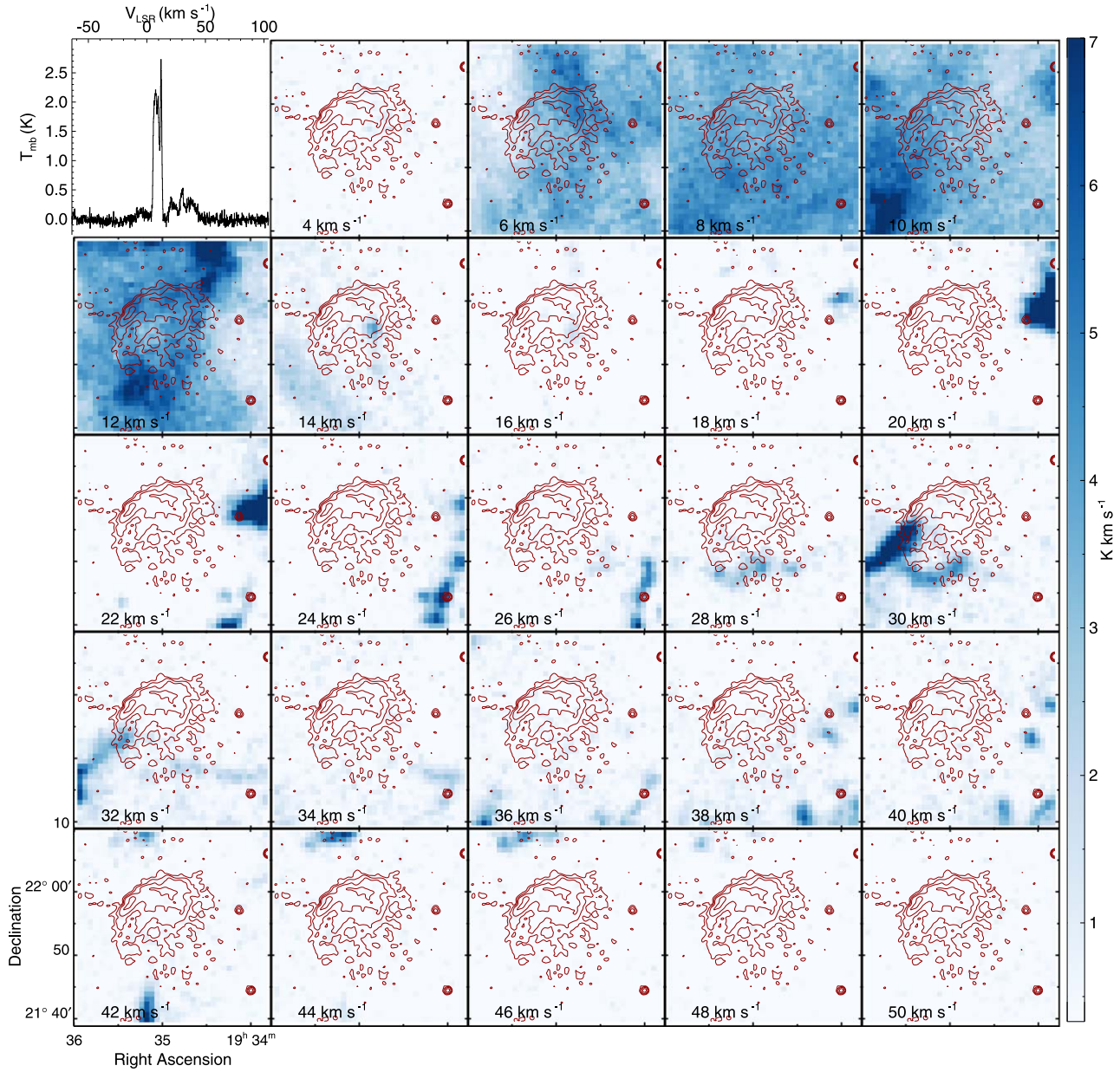

Figure 1. A grid of the velocity-integrated intensity maps of PMO ^{12}CO $J = 1$–0 emission with a velocity step of 2 km s^{-1}. The contours are taken from the THOR 1.4 GHz radio continuum. The first panel shows the ^{12}CO $J = 1$–0 spectrum averaged across the FOV.

km s^{-1}. Nevertheless, given the low sensitivity of the ^{13}CO emission, we do not know whether the ^{12}CO emission is indeed optically thin (e.g., with a large ^{12}CO/^{13}CO line ratio) or not. We saw line crowding in some regions in the FOV, where multiple line components are shown between $V_{\rm LSR} = 20$ and 45 km s^{-1}. For this reason, although the broad line at the molecular arc appears to be a single Gaussian, future molecular observations will be needed to test the line-crowding possibility. Therefore, based on this alone, we cannot rule out a broadening due to line-of-sight effects. We also plot in Figure 2 the ^{12}CO and ^{13}CO spectra from the inner shell region defined in Figure 3. We have not found any broadened lines in this region or other parts of the FOV. The narrow line in the inner shell and the maser point is about 2 times weaker than that from the arc-like structure. With the fainter CO emission, the potential broadened line emission is under our detection limit.

The CO gas at 30 km s^{-1} corresponds to either a near distance of $d \sim 2.5$ kpc or a far distance of ∼6.6 kpc. Since the SNR has been established to be farther than 4.5 kpc, an association between the CO and the SNR implies a distance of ∼6.6 kpc. Using the assumption of local thermal equilibrium, we estimated the H_2 column density of the $V_{\rm LSR} \sim 30$ km s^{-1} narrow component to be $N(H_2) \simeq 2.8 \times 10^{20}$ cm^{-2} and the mass to be $M(H_2) \simeq 200 d_{6.6}^2\, M_\odot$, where $d_{6.6} = d/(6.6\,{\rm kpc})$ (see Zhou et al. 2016). Assuming that the size of the ^{12}CO arc in the line of sight is the same as its width, the density of the narrow component is $n(H_2) = N(H_2)/{\rm depth} \simeq 20 d_{6.6}^{-1}$ cm^{-3}. The low mean density suggests that the MCs are highly clumpy and not resolved in the CO observations.

In Figure 3, we compare the molecular structures with the radio image of G57.2+0.8 and the mid-IR emission. In the radio band, G57.2+0.8 is limb brightened and has a faint spherical halo in the south (Sieber & Seiradakis 1984; Kothes et al. 2018).

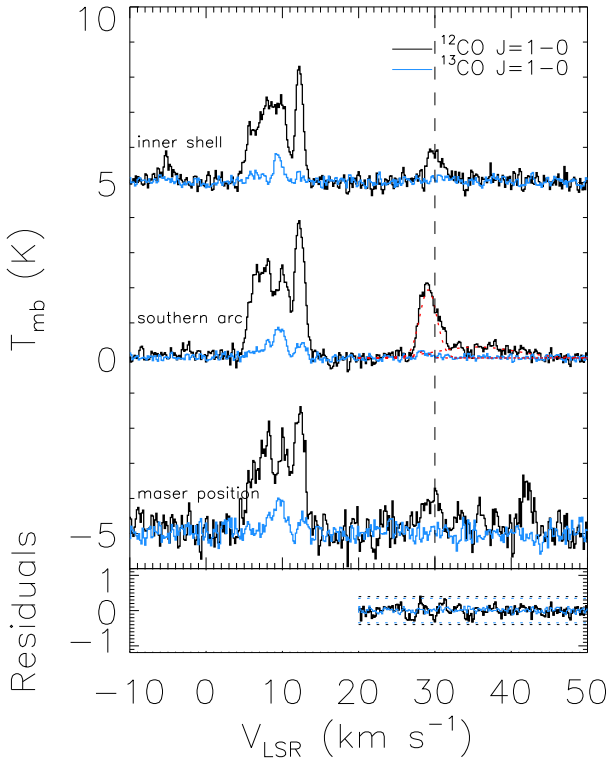

Figure 2. Spectra of the $J = 1$–0 transitions of ^{12}CO and ^{13}CO from the inner shell, southern arc-like region, and the maser position (see the regions labeled in Figure 3). The vertical dashed line denotes $V_{LSR} = 30$ km s^{-1}. The residual panel is given for the southern arc spectra fitted using two Gaussian lines (red dashed lines).

There is more than one explanation for the limb-brightened radio morphology. It could result from a density enhancement of the ambient medium in the northeast, which is, however, not seen in our molecular maps or H I map at $V_{LSR} \sim 30$ km s^{-1} (except for the inner shell, see the H I image in Figure 12 and relevant discussion in Appendix C). Although the CO emission at $V_{LSR} \sim 12$km s^{-1} is enhanced in the radio-brightened hemisphere of the SNR, we have not found physical evidence to support its association with the SNR. Kothes et al. (2018) found an H I cavity at $V_{LSR} \sim -46$ km s^{-1} morphologically enclosing the northeastern hemisphere of the SNR, also in need of kinematic evidence. The radio morphology could also result from an enhancement of the magnetic fields on one side (Orlando et al. 2007; West et al. 2016) or interaction with the winds of a runaway progenitor star (Zhang et al. 2018).

The spherical radio morphology indicates that SNR recently impacts with dense medium, which could be dense enough to deform the SNR morphology. The southern molecular arc does not confine the radio halo, but could be a structure behind the SNR, as indicated by the possible redshifted broad line (see Figure 2). The redshifted velocity is $\sim$6 km s^{-1}, lower than the blast wave velocity $v_s \lesssim 200$ km s^{-1} (see Section 4.2) and the cloud shock velocity $v_c \sim 12$ km s^{-1} implied by the broad ^{12}CO line. Assuming a ram pressure balance between the blast wave and the cloud shock, we have $n_c v_c^2 \sim n_0 v_s^2$ (McKee & Cowie 1975), where n_c and n_0 are the shocked cloud density and preshock intercloud density, respectively. Therefore, the cloud shock velocity is correlated to the density ratio between the preshock intercloud and shocked dense cloud: $v_c \lesssim 200(n_0/n_c)^{1/2}$ km s^{-1}. Although the density ratio is unclear (<1), both v_c and redshifted velocity values are in reasonable ranges.

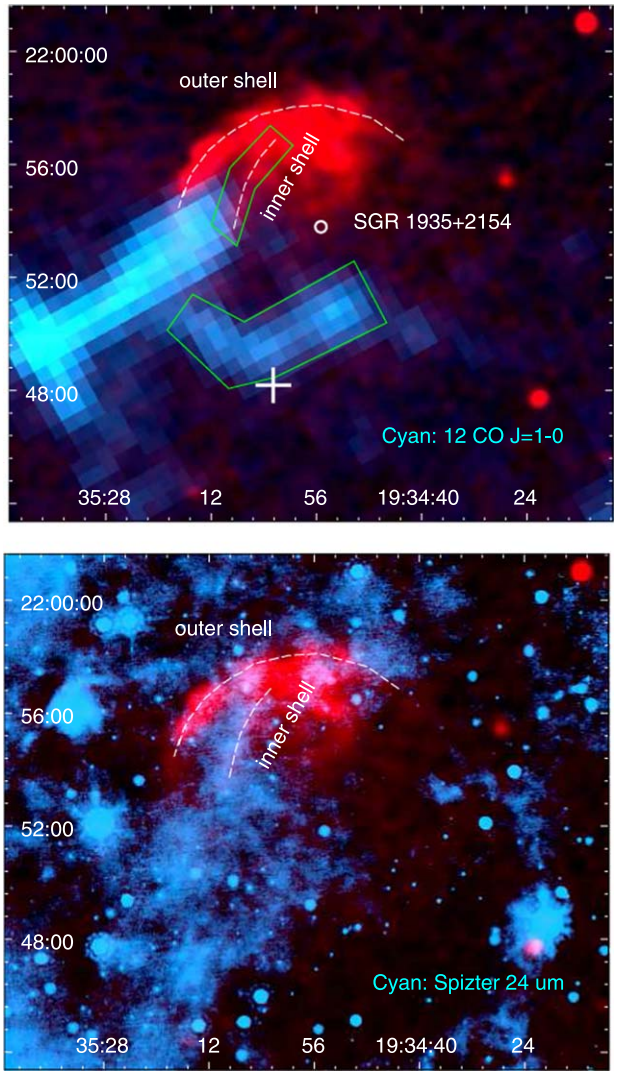

Figure 3. Composite images comparing the THOR 1.4 GHz radio continuum (red) and PMO ^{12}CO $J = 1$–0 (upper panel, cyan color; $V_{LSR} = 28$–32 km s^{-1}) or Spitzer 24 μm (lower panel, cyan color) emission. The polygons in the upper panel define the regions "inner shell" and "arc" for CO spectral extraction. The circle and cross signs denote the position of the magnetar and 1720 MHz OH maser.

The THOR radio image shows a relatively faint inner radio shell in the north, well correlated with the mid-IR 24 μm emission (see the lower panel of Figure 3). The spatial correlation between the two bands has been found in a number of SNRs that interact with dense medium (see Pinheiro Gonçalves et al. 2011; Koo et al. 2016, and references therein). The existence of an inner shell structure also favors an impact of shock with the dense gas in the foreground or background, similar to those found in SNR W28 (e.g., Frail et al. 1994; Claussen et al. 1997; Arikawa et al. 1999; Zhou et al. 2014). As shown in Figure 3, the eastern molecular bar ends at the inner radio shell, consistent with the picture that an interaction with dense medium causes the inner shell.

3.2. 1720 MHz OH Maser

1720 MHz OH masers, when unaccompanied by the other ground-state transitions at 1662, 1665, and 1667 MHz that are usually pumped by a far-IR radiation field, are regarded as

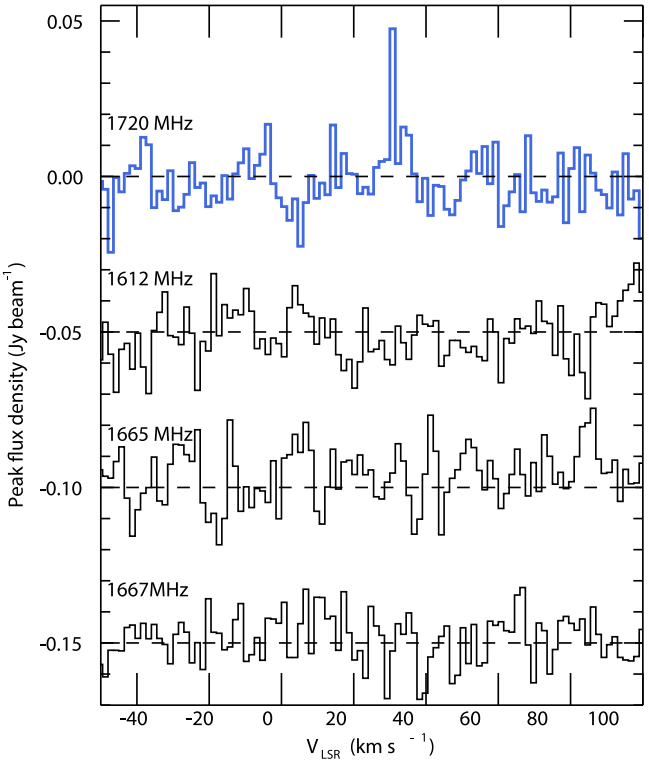

Figure 4. Spectra of four ground-state transitions of OH at the position $19^{h}35^{m}02\overset{s}{.}84$, $21°48'11\overset{''}{.}59$ (J2000; see the cross in Figures 3 and 5).

signposts of the collision between shock and MCs (e.g., Frail et al. 1994; Claussen et al. 1997; Wardle & Yusef-Zadeh 2002). Compared to the thermally excited OH emission, OH masers are narrow (generally $\lesssim$2 km s^{-1}; Claussen et al. 1997), compact, and too bright to be explained as thermal lines.

From the THOR OH survey, we have found a 1720 MHz line at the southern radio boundary of G57.2+0.8 at $V_{\rm LSR}$ = 30 km s^{-1} (see Figure 4, from the OH tile centered at $l = 56\overset{\circ}{.}75$). The line is identified from a spatially unresolved region and shown in two tiles of OH data cleaned separately. The cleaning areas of the two tiles center at $l = 56\overset{\circ}{.}75$ and 58°, respectively, with a size of 4° × 2°.5, while other cleaning parameters are the same and the data were from the same survey (see Beuther et al. 2016 for details). The line is also narrow, as the line profile is unresolved with the velocity resolution of 1.5 km s^{-1}. Moreover, we have not found accompanied 1612, 1665, and 1667 MHz OH lines at the position and LSR velocity. The peak flux densities of the 1720 MHz OH line are 47 and 44 mJy beam^{-1} in the tiles centered at $l = 56\overset{\circ}{.}75$ and 58°, respectively, corresponding to a high radiation temperature of ∼130 K for a given beamwidth of 12″. The radiation temperature is significantly larger than the ^{12}CO temperature along the line of sight. All of these properties suggest that the line is a collisionally excited OH maser.

The OH maser was not reported before, probably because previous surveys did not have the required sensitivity (25 mJy in Hewitt et al. 2009) or the line is too narrow. We note that 1720 MHz maser is only detected in a single velocity-channel, which could be caused by the narrow width of the OH maser. The maser was not listed in the OH maser catalog compiled in Beuther et al. (2019), which selected masers with >2 rms detection in more than one velocity-channel. The two-channel criterion in Beuther et al. (2019) is used to reduce sporadic false detection and ensure clean detection. However, it could result in incomplete detection because it tends to omit narrow and faint masers. Narrow 1720 MHz OH masers with width $\leqslant$1.5 km s^{-1} have been extensively found in SNRs. Claussen et al. (1997) show that around half of the OH masers in W44 and W28 are narrower than 1 km s^{-1} or detected in less than three channels (channel resolution of 0.53 km s^{-1}). The 1720 MHz OH line near G57.2+0.8 matches all the other criteria in Beuther et al. (2019), given its $\gtrsim$5 rms intensity at a single position and its brightness of >20 mJy beam^{-1} in over 12 pixels (pixel size of 3″). The rms value is determined using the OH spectrum at the maser spot (see Appendix A for details). Moreover, the maser's position is coincident with the radio boundary of G57.2+0.8 and its velocity is consistent with that of the ^{12}CO arc.

In Appendix A, we provided details of the maser identification and its likelihood. We have calculated the chance coincidence of an OH spot randomly falling in the SNR, using the real 1720, 1612, 1665, and 1667 MHz data in a sky region 16.4 times that of the SNR area. We considered the rms distribution in the spatial and channel dimensions. Subsequently, we calculated how frequently an OH spot at a random velocity corresponds to ^{12}CO emission. A false OH spot would be found at any velocity channel and does not need to correspond to ^{12}CO emission. The chance coincidence of a maser spot in the SNR is $\leqslant$12% at the detected maser's significance level, and the chance of OH–CO correspondence is 7%. The two probabilities are multiplied to give the probability for a false OH spot in the SNR that happens to correspond to MCs. As a result, the false detection probability is <1%, suggesting a real detection.

The maser position is located at the outer boundary of the molecular arc and lies away from the radio-bright shell (see Figure 3(a)). The location could be due to the projection effect or/and a favorable excitation condition (Lockett et al. 1999). Masers are highly beamed emission. It is more likely to observe masers near the SNR boundary, because the collisionally excited masers are beamed toward the observer who views the shock "edge-on" (e.g., Hollenbach et al. 2013). The angular resolution of the PMO ^{12}CO data is around 1′ (∼1 $d_{6.6}$ pc), much larger than the maser or maser groups (10–10^3 au; Elitzur 1992; Beuther et al. 2019). The ^{12}CO emission across the SNR is much weaker than the typical dense MCs (∼10 K; see, e.g., Draine 2011), indicating that the gas is highly clumpy and unresolved using the PMO observation. Consequently, the beam dilution causes a weak CO emission. This also prevents us from deriving the temperature, density, and column density of the molecular core that produces the OH maser. Figure 2 shows that our PMO CO observation is not sensitive enough to detect weak, broadened CO emission at the maser point. Future high-resolution and high-sensitivity observations are needed to search for broadened molecular emission at the maser point. Nevertheless, earlier 1720 MHz OH maser surveys in SNRs have revealed that the masers do not always correspond to the radio or CO peaks. Instead, they could appear at radio-faint structures (Frail et al. 1996; Hewitt et al. 2009) or CO-weak regions (e.g., 3C391, N49; Frail et al. 1996; Brogan et al. 2004). A cluster of masers has also been found in the outer boundaries of the MCs in W28 and W44 (see Figure 1 in Frail & Mitchell 1998). The CO and maser emission together provide evidence for an SNR–MC interaction, with the SNR being located at ∼6.6 kpc.

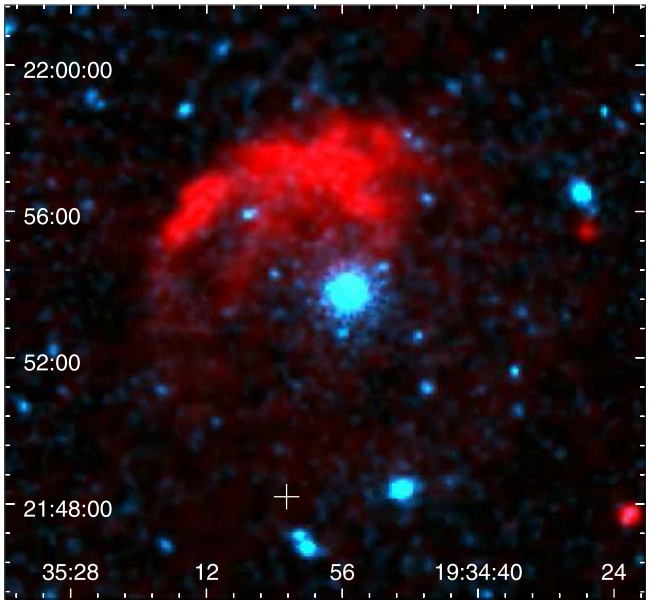

Figure 5. A composite image of G57.2+0.8 in the XMM-Newton X-ray (cyan; 0.4–7.2 keV) and THOR 1.4 GHz radio bands (red). SGR 1935+2154 is the bright X-ray source in the center. The cross sign in the south denotes the position of the 1720 MHz OH maser.

3.3. X-Ray Analysis

Figure 5 shows the 0.4–7.2 keV X-ray emission of G57.2 +0.8 and SGR 1935+2154, with the VLA 1.4 GHz continuum coded in red for comparison. We have not found any evidence of the extended X-ray emission from the shell or the interior of the SNR. Considering that the SNR is interacting with a dense medium, the nondetection of X-ray emission is not because of the low gas density, but suggests that the shock velocity is too low to heat the gas to the high temperature.

4. Discussion

4.1. Distance

We have shown that G57.2+0.8 is likely associated with CO gas and excites a 1720 MHz OH maser at $V_{\rm LSR} \sim 30$ km s^{-1}. This LSR velocity corresponds to a kinematic distance of 6.6 ± 0.7 kpc according to the rotation curve of the Galaxy (Reid et al. 2014), where the uncertainty is given at the 1σ level based on the Monte Carlo method by Wenger et al. (2018). The distance falls within the lower and upper limits (4.5–10 kpc) constrained using the H I absorption method (Ranasinghe et al. 2018) and the magnetar's blackbody emission (Kozlova et al. 2016), respectively.

4.2. SNR Properties

We herein update the SNR age t using the new distance. The nondetection of the X-ray emission (see Figure 5) supports that the SNR gas has significantly cooled. Therefore, it is reasonable to consider the SNR has reached the radiative phase, as suggested by Kothes et al. (2018). During this phase, the SNR expansion is pressure driven, having a solution $R_{\rm s} \propto t^{0.31}$ (Chevalier 1974), where the SNR radius $R_{\rm s} = 10.6 d_{6.6}$ pc for an angular radius of 5.′5. Using an upper limit of the shock velocity v_s of 200 km s^{-1} in the radiative phase (Vink 2012), the SNR age is estimated as $t = 0.31 R_{\rm s}/v_s > 1.6 \times 10^4 d_{6.6}$ yr. This is still larger than the characteristic age of SGR 1935+2154 obtained from the spin properties (3600 yr; Israel et al. 2016). However, as pointed out in previous studies (e.g., Olausen & Kaspi 2014; Kothes et al. 2018), the characteristic ages are poor age indicators, while SNR ages better represent the real ages of the magnetars.

The explosion energies of magnetars in SNRs have been found to vary by over one order of magnitude (Vink & Kuiper 2006; Zhou et al. 2019). Particularly, SNR RCW 103 hosting the magnetar 1E 161348−5055 originated from a very low energy explosion ($\sim 10^{50}$ erg; Braun et al. 2019; Zhou et al. 2019). Therefore, we cannot simply assume a canonical explosion energy $E = 10^{51}$ erg for G57.2+0.8 and SGR 1935+2154. The explosion energy of an SNR in the radiative phase can be estimated as $E = 1.5 \times 10^{50} n_0^{1.16} (R_{\rm s}/10.6\ {\rm pc})^{3.16} (v_{\rm s}/200\ {\rm km\ s^{-1}})^{1.35}$ erg (Cioffi et al. 1988), where n_0 is the mean density of the ambient gas. We do not expect the n_0 value to be as large as the MC density $n({\rm H_2}) \sim 20$ cm^{-3}. The progenitors of magnetars are massive stars, whose stellar winds can create large low-density bubbles before the supernova explosions (Chevalier 1999; Chen et al. 2013). As shown in Figure 5, the radio morphology of G57.2+0.8 is almost round (although limb brightened) and MCs overlap only a small portion of the SNR. This is consistent with the scenario that the SNR was initially evolved in a homogeneous, low-density medium until it reached the dense molecular gas. If we use a large mean ambient gas density $n_0 = 10$ cm^{-3}, we derived the explosion energy of G57.2+0.8 as $< 2.1 \times 10^{51} d_{6.6}^{3.16}$ erg. Given the distance and low SNR velocity, SGR 1935+2154 is unlikely to be formed from a very energetic explosion, consistent with those in other magnetars in SNRs (Vink & Kuiper 2006; Martin et al. 2014; Zhou et al. 2019).

5. Conclusion and Remarks

Here we summarize the results from the multiwavelength study and our concerns about the uncertainties of the observational results. We have performed molecular environment study of G57.2+0.8 and found that the MCs at $V_{\rm LSR} = 6$–14 km s^{-1} and 30 km s^{-1} are spatially overlapping the SNR. The physical interaction between the SNR and MCs is mainly built on a single, weak 1720 MHz maser detected at $V_{\rm LSR} = 30$ km s^{-1}, as 1720 MHz OH masers are regarded as signposts of shock–cloud interaction. Moreover, the spatial correlation between the inner shell and mid-IR emission, and the existence of MC connecting to the inner shell at $V_{\rm LSR} \sim 30$ km s^{-1}, provides additional morphological support. Nevertheless, we are aware that further high-resolution molecular observation is needed to provide more kinematic evidence and confirm this association. We have analyzed the XMM-Newton X-ray data to search for thermal X-ray emission from G57.2+0.8. The nondetection of X-ray emission suggests that the SNR is old.

Based on the LSR velocity of the MCs, we derived a kinematic distance of G57.2+0.8 as 6.6 ± 0.7 kpc. We also constrained the SNR age to be larger than $1.6 \times 10^4 d_{6.6}^{-1}$ yr and the supernova explosion energy to be less than $2.1 \times 10^{51} d_{6.6}^{3.16}$ erg. These properties are shared between G57.2+0.8 and SGR 1935+2154.

We thank Hao Qiu for discussion on FRBs and thank Sera Markoff and Vladimír Domček for helpful comments. P.Z. acknowledges the support from the Nederlandse Onderzoekschool Voor Astronomie (NOVA) and NWO Veni Fellowship. This work is supported by National Key R&D Program of China grants Nos. 2017YFA0402701 and 2017YFA0402600,

and Key Research Program of Frontier Science, CAS, grant No. QYZDJ-SSW-SLH047, and NSFC grants Nos., 11503008, 11590781, 11403104, 11773014, 11633007 & 11851305. J.S. W. is supported by China Postdoctoral Science Foundation. Y.W. acknowledges support from the European Research Council under the Horizon 2020 Framework Program via the ERC Consolidator Grant CSF-648505.

Software: GILDAS (https://www.iram.fr/IRAMFR/GILDAS/), SAS (https://www.cosmos.esa.int/web/xmm-newton/download-and-install-sas), DS9 (http://ds9.si.edu/site/Home.html), Starlink (Currie et al. 2014).

Appendix A
The Reliability of the 1720 MHz OH Maser Detection

The 1720 MHz OH maser at the position ($19^h35^m02^s.84$, $21°48'11''.59$, J2000) is narrow and weak, with a peak flux density of 47 mJy beam^{-1} in the data tile centered at $l = 56.^\circ75$. It is found at the boundary of the SNR and coincides with CO emission. The cleaning setup influences the noise distribution of the interferometric data. The cleaning-introduced noise could disappear in other data with a different cleaning area. We took the neighboring tile at $l = 58°$ and also detected the maser at the same position and velocity with a peak flux density of 44 mJy beam $^{-1}$. The data of the two tiles were taken from the same survey, but the areas used for cleaning shifted by $1.^\circ25$. As the tiles at $l = 58°$ and $l = 56.^\circ75$ (the one used in the paper) were cleaned separately, it is highly unlikely the cleaning-introduced noise spot would be at the same position and velocity. Hereafter we calculate the probability for a false detection randomly coincident with the SNR.

We first identified OH spots from a large-scale region centered at ($l = 57.^\circ235$, $b = 0°$) with a size of $13' \times 2°$. We selected a region along the latitude because the rms along the longitude has a large variation (see Figure 6), and because identifying clumps in a very large region requires computing resources. Two tiles with different cleaning areas are cross-matched to filter out cleaning-introduced noise. The identified clumps are used to give the probability for an OH clump falling in the SNR (P_1). Subsequently, we examined the ^{12}CO data cube and checked the probability of an OH line that happens to overlay a CO line (P_2).

We identified clumps in the 1720 MHz OH data cube in each velocity channel from -58.5 to 135 km s^{-1} by applying the FellWalker clumpfind algorithm (Berry 2015) in the STARLINK package. The search criteria include at least 12 pixels in a single channel, with over 2σ detection. These criteria are similar to those in Beuther et al. (2019), but we identified spots in the single channel for narrow lines, searched for clumps with larger significance levels, and used two tiles of data for cross-matching. Beuther et al. (2019) show that no masers are detected in over two consecutive velocity channels in this sky region. This over two-channel criterion is used to reduce spurious detection, but it could omit narrow masers.

There is a spatial variation of the rms across the field, which influenced the significance level of the identified clumps and should be considered. We calculated the rms in each pixel using all velocity channels and obtained the minimum, mean, and maximum rms values of 5.61 mJy, 8.78 mJy, and 12.5 mJy, respectively, for the tile at $l = 56.^\circ75$. We also found a variation of rms with the velocity channel (generally $<10\%$, but could be over 20% in some pixels). In general, the larger rms is found in the edge channels for 1720 MHz OH data, especially channels with velocities >80 km s^{-1} (see Figure 7), but the rms (channel) shape varies across the data. Here we searched for maser spots in two rms cases. In Case A, we only consider the spatial rms variation. In Case B, we take the channel-dependent variation of rms into account. The rms in each channel was then calculated using the 40 neighboring channels. In the 20 edge channels, the rms might have larger uncertainties as more data were taken from one side.

A.1. Case A

Assuming that the noise is independent of the velocity channel, we found all of the detected spots with $|S/N| < 5.4$. We searched for clumps with peak values with signal-to-noise ratio (S/N) = 4.5–6 and −6–4.5. The spots with negative S/N and flux are false detection and are used to test the noise distribution as a function of S/N. Figure 8 shows the detection number in the $13' \times 2°$ region and the fraction of the identified clumps in the SNR given the area ratio. The black line shows the results from the tile at $l = 56.^\circ75$ alone, while the blue shaded area shows the cross-matched detection using both tiles at $l = 56.^\circ75$ and $l = 58°$. The figure proves that over 3/4 of the identified spots with S/N < 5 are false signals due to different cleaning areas. None of the S/N $\geqslant$ 4.7 spots have 1612/1665/1667 OH counterparts. The two panels in Figure 8 show that positive and negative noise distribution is nearly symmetric. They show that $|S/N| \sim 5$ approaches the end of the noise tail.

At the significance of 4.95, we identified three spots in the large region (16.4 times the SNR area), including the $V_{LSR} = 30$ km s^{-1} spot at the boundary of G57.2+0.8. For comparison, there are two confirmed noise spots with S/N < −4.95. Assuming that all the identified spots are false signals, for randomly finding one spot with a peak significance of 4.95 in both tiles in an area as large as the SNR, the probability is only 18% (12% when considering the spots with negative values).

As OH is a molecule, the real OH line is expected to correspond to molecular emission at around the same LSR velocity. In contrast, the false detection would have a randomly

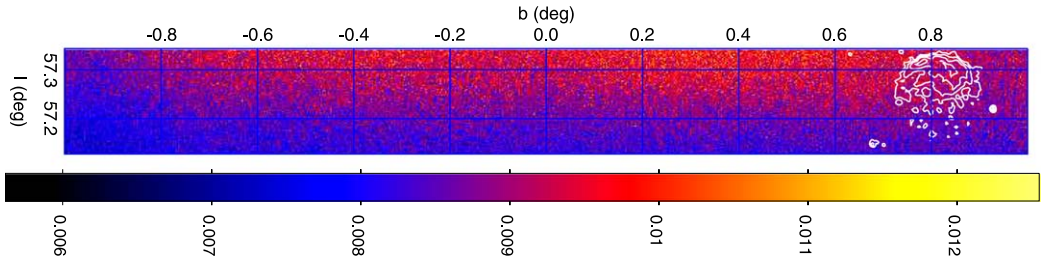

Figure 6. The rms distribution of the 1720 MHz OH data in the large-scale region centered at ($l = 57.^\circ235$, $b = 0°$) with a size of $13' \times 2°$. The radio contours of G57.2+0.8 are overlaid. The unit of the color bar is Jy beam^{-1}. The Galactic longitude (l) and latitude (b) axes are rotated.

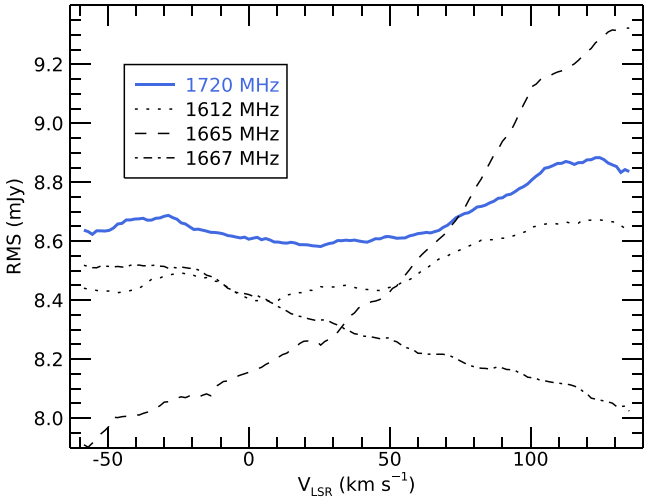

Figure 7. The channel-dependent rms of the 1720/1612/1665/1667 MHz OH data, averaged across the large-scale region.

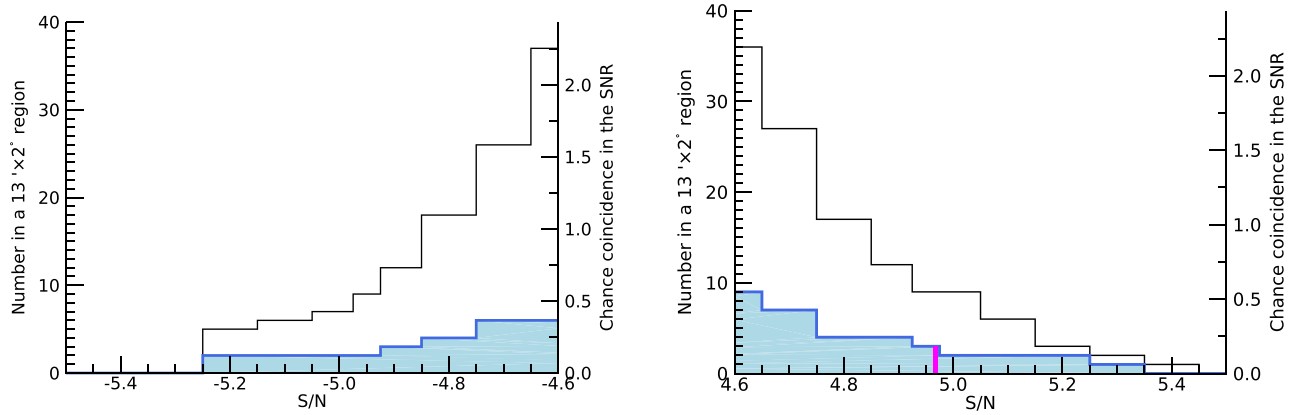

Figure 8. The identified 1720 MHz OH spots in a $13' \times 2°$ region with S/N in the range of -5.5 to -4.6 (left panel) and 4.6–5.5 (right panel), assuming that the noise is independent of the velocity channel (Case A). The left and right axes give the detection number and the chance coincident rate in the SNR. The black line shows the identified number in from the single tile $l = 56.^{\circ}75$, which suffered extra noise due to the cleaning of the interferometric data. The blue line with the shaded region shows the identified spots in both tiles. The magenta vertical line denotes the lower limit of the S/N for the $V_{LSR} = 30$ km s^{-1} maser spot in both tiles at $l = 58°$ and $56.^{\circ}75$, respectively.

distributed V_{LSR} and does not need a ^{12}CO counterpart. At the position of the 1720 MHz OH maser near G57.2+0.8, only ~7% of channels have over 3σ ^{12}CO emission in $V_{LSR} = -58.5$–135 km s^{-1}. We retrieved PMO ^{12}CO $J = 1$–0 data for a large sky region centered at $l = 57.^{\circ}235$, $b = 0.^{\circ}68$ and with a size of $13' \times 1°$. We found that the over 3σ ^{12}CO line is shown in <22% (mean value of 6.7%) of the velocity channels. This means the probability for an OH–^{12}CO coincidence is low and can be used to filter out false detection.

At the 4.95σ level, the probability of an OH spot randomly falling in the SNR is $P_1 = 18\%$, and the probability of OH–^{12}CO correspondence is $P_2 = 7\%$. As P_1 and P_2 are independent, the false detection rate is $P_f = P_1P_2 \sim 1\%$ for the 1720 MHz OH spot that we identified at the boundary of G57.2+0.8. Therefore, the probability of the real detection of the 1720 MHz maser is roughly estimated as $P = 1 - P_f \sim 99\%$. Nevertheless, the next two subsections will show that the channel-dependent rms variation indeed changes the results and should be considered.

A.2. Case B

We repeated the clump identification process, but including the variation of rms with velocity channels. Figure 9 shows the identified clumps. The $V_{LSR} = 30$ km s^{-1} maser spot near G57.2+0.8 is identified in both tiles and is the only spot with a minimum S/N = 6.4. The S/N of the spot is larger than in Case A, as the rms at $V_{LSR} = 30$ km s^{-1} is generally lower than the edge channels. We noted that the noise distribution of Case B is less symmetric than Case A and the negative noise tail extends to the larger |S/N|. Nevertheless, in Case B, the S/N of our maser spot is still at the end of the noise tail, and the chance coincidence in the SNR is still low ($P_1 = 6\%$). In this case, the probability of the real detection of 1720 MHz maser in the SNR is $P = 1 - P_1P_2 = 99.6\%$.

A.3. Spot Identification in 1612/1665/1667 MHz OH Data

For comparison purposes, we searched for OH clumps using 1612, 1665, and 1667 MHz THOR data and checked their S/N distributions. The identification processes are the same as that for the 1720 MHz OH data. Figure 10 shows the identified positive-flux spots as a function of the S/N. For Case A, at the significance of 4.95, the chance coincidence in the SNR P_1 is 6%, 55%, and 12% for 1612, 1665, and 1667 MHz OH data, respectively. The 1665 MHz data have a significantly larger detection than other data, due to the channel-dependent rms

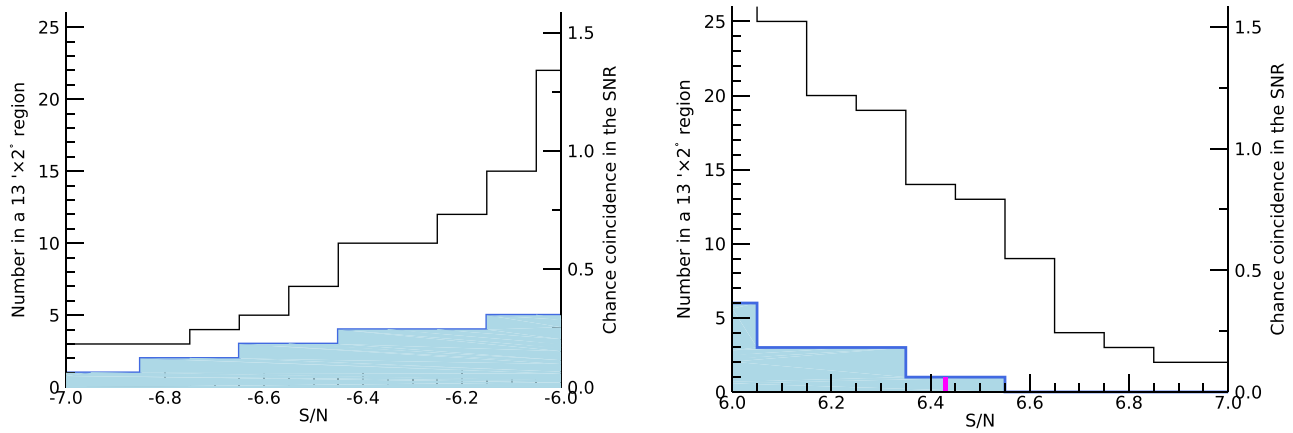

Figure 9. The figure is similar to Figure 8, but the spot identification considers the varied noise across the velocity channels.

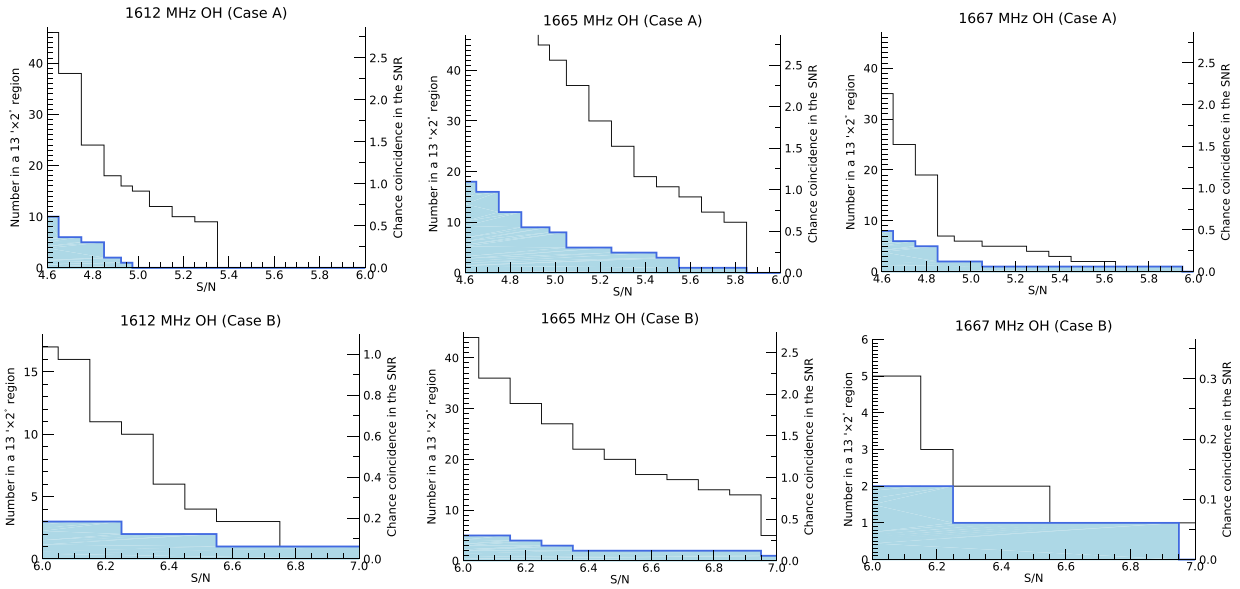

Figure 10. The images are similar to the right panels of Figures 8 and 9, but for three other OH transitions.

distribution. Eight in nine spots are at $V_{\rm LSR} > 88$ km s^{-1}, where the rms is larger than the mean rms level (see Figure 7). This favors Case B as a meaningful case.

In Case B, at the significance of 6.4, the chance coincidence for a random spot found in the SNR P_1 is 12%, 12%, and 6% for 1612, 1665, and 1667 MHz data for the full channels. The P_1 values are similar to the number of 6% for 1720 MHz data. All of the identified spots at around edge channels with the LSR velocities larger than 88 km s^{-1} or smaller than -42 km s^{-1}, where the rms is enhanced (see Figure 7).

The comparison between Cases A and B shows that the spots tend to be identified at the channels with underestimated rms. If we exclude the edge channels with high rms and only consider the velocities in -42–88 km s^{-1}, the 1720 MHz OH spot near G57.2+0.8 is the only identified spot with S/N > 6.4 among all THOR OH data. We verify that only one spot among the four 1720 MHz OH spots with S/N < -6.4 falls in this velocity range. This reinforces a larger chance to find spots in these edge channels.

We conservatively set the chance coincidence P_1 to 12%, using the upper limit in four groups of OH data and considering all channels, although the false rate should be much lower as all the other spots are detected at round edge channels.

The above analysis provides evidence that the 1720 MHz OH maser spot near G57.2+0.8 is not a random OH noise that happens to correspond to ^{12}CO emission. Although it is faint, the false possibility is only <1% (P_1P_2). Actually, faint and narrow 1720 MHz OH masers have also been found in other SNRs. Hewitt et al. (2009) detected two faint OH masers with a peak flux less than 70 mJy beam^{-1}. Two faint 1720 MHz OH masers were detected in N49 (Brogan et al. 2004), which is an SNR hosting magnetar SGR 0526−66. The brighter maser in N49 has a peak flux density of 35 mJy beam^{-1} and has a line width less than 1 km s^{-1}, even weaker than that reported here.

Appendix B
Line Widths of the OH Maser

The OH maser near G57.2+0.8 is only detected in a single channel due to the narrow line width. Here we examined whether the line wing could be bright enough to be detected in the adjacent channels if the line peak is at the channel center. Figure 4 shows that the observed line wing of the maser is at

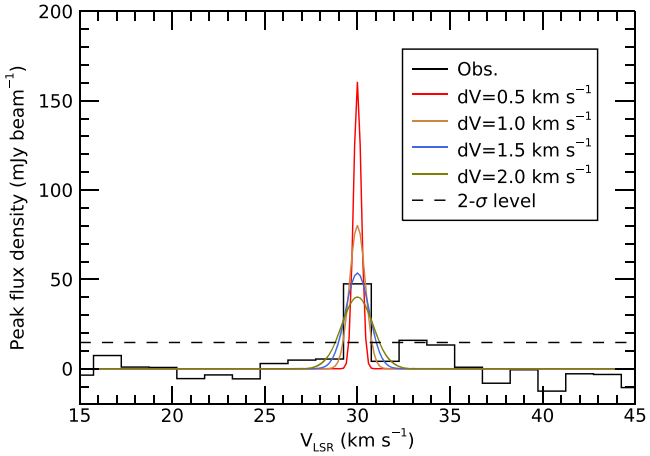

Figure 11. A comparison of the observed 1720 MHz OH maser and a few Gaussian lines with different line widths but the same area as that of the observed line.

$<1\sigma$ level, below the detection level. Considering the line peak is at 6.4σ level, we expect to detect >76% flux in the central channel. According to the Gauss error function, the flux fraction is $\mathrm{erf}(z/\sqrt{2}) > 0.76$, which gives $z < 1.175$. The value z can be expressed using the channel resolution $dV_c = 1.5$ km s^{-1} and the FWHM of the line dV: $z = \sqrt{2\ln 2}\,dV_c/dV$. Therefore, we obtained $dV < 1.5$ km s^{-1}. Setting the wing-channel significance at 2σ will give $z \leqslant 0.87$ and a line width $dV \leqslant 2$ km s^{-1}. If the line centroid mismatches the channel center, then the line width should be lower than the aforementioned values.

Figure 11 shows the observed spectrum and four exemplified Gaussian lines with a velocity-integrated flux density equal in area of the three channels (85.6 mJy beam^{-1} km s^{-1}). The figure displays that lines with widths $dV \leqslant 1.5$ km s^{-1} may not be detected in more than one channel, as the line wings are too faint.

Appendix C
H I Morphology at $V_{\rm LSR} = 29.5$ km s^{-1}

As shown in Figure 12, the H I morphology at $V_{\rm LSR} = 29.5$ km s^{-1} is relatively smooth, with a bright knot in the SNR north. There are two possible explanations for the lack of structured H I emission at $V_{\rm LSR} \sim 30$ km s^{-1}. The first possible reason is that G57.2+0.8 is not in an atomic environment. So far, the H I studies of G57.2+0.8 have not provided any kinematic evidence to support that SNR G57.2+0.8 perturbs or heats H I gas (see Surnis et al. 2016; Kothes et al. 2018; Ranasinghe et al. 2018). Although a morphological match between a H I structure at $V_{\rm LSR} = -46$ km s^{-1} and the SNR has been proposed (Kothes et al. 2018), the chance coincidence has not been ruled out. We have not found relevant CO structures at $V_{\rm LSR} = -46$ km s^{-1} (see Figure 13). In the alternative scenario, the SNR is in a relatively homogeneous atomic environment, and it is difficult to identify a shocked H I structure. The H I emission line is broad in the inner Galaxy, and the line crowding is severe. The right panel of Figure 12 shows that there are multiple H I components from $V_{\rm LSR} = -100$ km s^{-1} to 60 km s^{-1} toward G57.2+0.8. The H I morphology in a single channel can be easily contaminated by H I wings of nearby velocity components. In this case, an H I enhancement might not be discerned even if the SNR heats the atomic gas. A detailed exploration of shocked H I emission is out of the scope of this paper. From the H I images, we cannot conclude or refute a relationship between the SNR and the atomic gas at $V_{\rm LSR} \sim 30$ km s^{-1}.

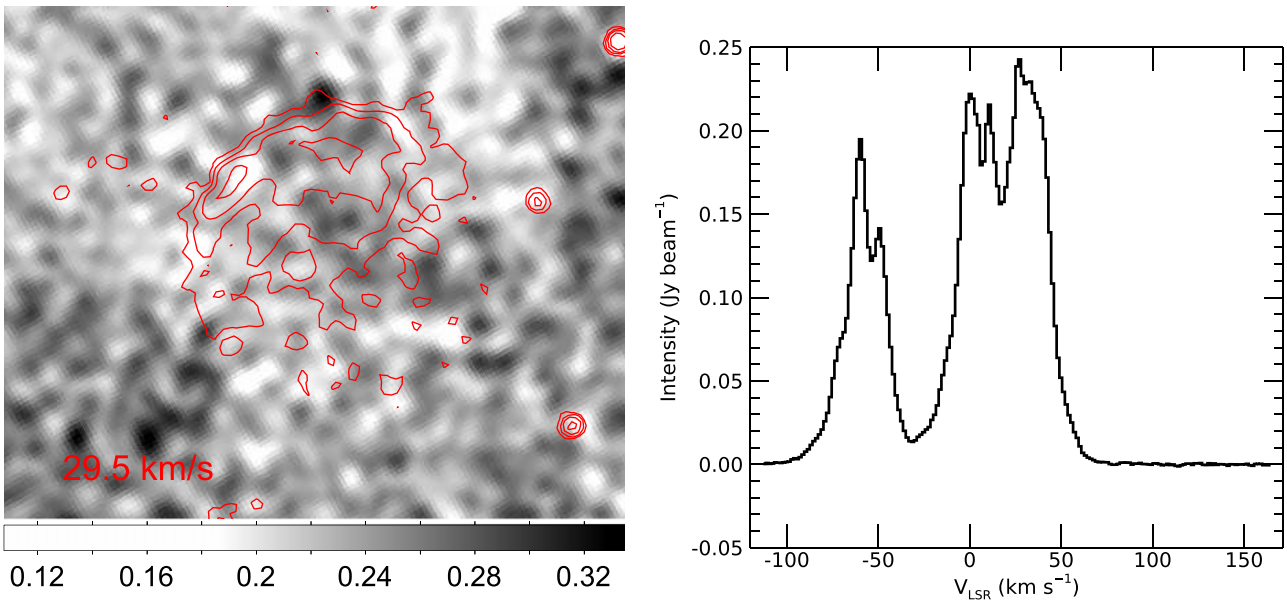

Figure 12. Left: H I morphology at 29.5 km s^{-1}. The unit of the color bars is Jy beam^{-1}. Right: averaged H I spectrum extracted from the SNR with a radius of 5.′5.

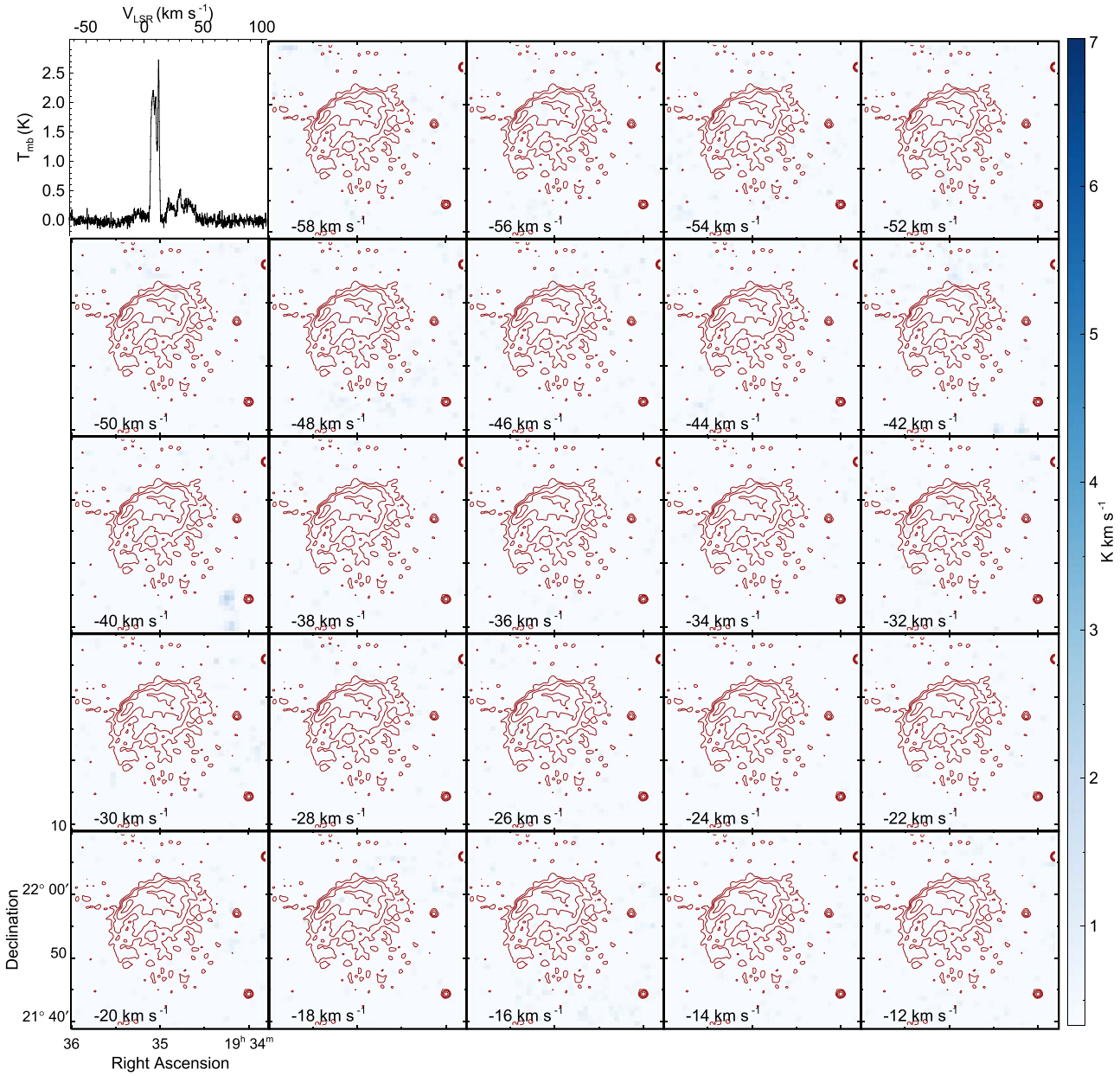

Figure 13. A grid of the velocity-integrated intensity maps of PMO ^{12}CO $J = 1$–0 emission in $V_{LSR} = -59$ to -11 km s^{-1} with a velocity step of 2 km s^{-1}. The contours are taken from the THOR 1.4 GHz radio continuum. The first panel shows the ^{12}CO $J = 1$–0 spectrum averaged across the field of view.

ORCID iDs

Ping Zhou https://orcid.org/0000-0002-5683-822X
Xin Zhou https://orcid.org/0000-0003-2418-3350
Yang Chen https://orcid.org/0000-0002-4753-2798
Jie-Shuang Wang https://orcid.org/0000-0002-2662-6912
Jacco Vink https://orcid.org/0000-0002-4708-4219

References

Arikawa, Y., Tatematsu, K., Sekimoto, Y., & Takahashi, T. 1999, PASJ, 51, L7
Barthelmy, S. D., Bernardini, M. G., D'Avanzo, P., et al. 2020, GCN Circ., 27657, https://gcn.gsfc.nasa.gov/gcn3/27657.gcn3
Berry, D. S. 2015, A&C, 10, 22
Beuther, H., Bihr, S., Rugel, M., et al. 2016, A&A, 595, A32
Beuther, H., Walsh, A., Wang, Y., et al. 2019, A&A, 628, A90
Bochenek, C. D., Ravi, V., Belov, K. V., et al. 2020, Natur, 587, 59
Braun, C., Safi-Harb, S., & Fryer, C. L. 2019, MNRAS, 489, 4444
Brogan, C. L., Goss, W. M., Lazendic, J. S., & Green, A. J. 2004, AJ, 128, 700
Chen, Y., Jiang, B., Zhou, P., et al. 2014, in IAU Symp. 296, Supernova Environmental Impacts, ed. A. Ray & R. A. McCray (Cambridge: Cambridge Univ. Press), 170
Chen, Y., Zhou, P., & Chu, Y.-H. 2013, ApJL, 769, L16
Chevalier, R. A. 1974, ApJ, 188, 501
Chevalier, R. A. 1999, ApJ, 511, 798
Cioffi, D. F., McKee, C. F., & Bertschinger, E. 1988, ApJ, 334, 252
Claussen, M. J., Frail, D. A., Goss, W. M., & Gaume, R. A. 1997, ApJ, 489, 143
Cummmings, J. R., Barthelmy, S. D., Chester, M. M., & Page, K. L. 2014, ATel, 6294, www.astronomerstelegram.org/?read=6294
Currie, M. J., Berry, D. S., Jenness, T., et al. 2014, in ASP Conf. Ser. 485, Astronomical Data Analysis Software and Systems XXIII, ed. N. Manset & P. Forshay (San Francisco, CA: ASP), 391
Draine, B. T. 2011, Physics of the Interstellar and Intergalactic Medium (Princeton, NJ: Princeton Univ. Press)
Elitzur, M. 1992, ARA&A, 30, 75
Fletcher, C. & Fermi GBM Team 2020, GCN Circ., 27659, https://gcn.gsfc.nasa.gov/gcn3/27659.gcn3

Frail, D. A., Goss, W. M., Reynoso, E. M., et al. 1996, AJ, 111, 1651
Frail, D. A., Goss, W. M., & Slysh, V. I. 1994, ApJL, 424, L111
Frail, D. A., & Mitchell, G. F. 1998, ApJ, 508, 690
Gaensler, B. M. 2014, GCN Circ., 16533, https://gcn.gsfc.nasa.gov/gcn3/16533.gcn3
Hewitt, J. W., Yusef-Zadeh, F., & Wardle, M. 2009, ApJL, 706, L270
Hollenbach, D., Elitzur, M., & McKee, C. F. 2013, ApJ, 773, 70
Israel, G. L., Esposito, P., Rea, N., et al. 2016, MNRAS, 457, 3448
Jiang, B., Chen, Y., Wang, J., et al. 2010, ApJ, 712, 1147
Koo, B.-C., Lee, J.-J., Jeong, I.-G., Seok, J. Y., & Kim, H.-J. 2016, ApJ, 821, 20
Kothes, R., Sun, X., Gaensler, B., & Reich, W. 2018, ApJ, 852, 54
Kozlova, A. V., Israel, G. L., Svinkin, D. S., et al. 2016, MNRAS, 460, 2008
Larson, R. B. 1981, MNRAS, 194, 809
Li, C. K., Lin, L., Xiong, S. L., et al. 2020, arXiv:2005.11071
Lockett, P., Gauthier, E., & Elitzur, M. 1999, ApJ, 511, 235
Martin, J., Rea, N., Torres, D. F., & Papitto, A. 2014, MNRAS, 444, 2910
McKee, C. F., & Cowie, L. L. 1975, ApJ, 195, 715
Mereghetti, S., Savchenko, V., Ferrigno, C., et al. 2020, ApJL, 898, L29
Olausen, S. A., & Kaspi, V. M. 2014, ApJS, 212, 6
Orlando, S., Bocchino, F., Reale, F., Peres, G., & Petruk, O. 2007, A&A, 470, 927
Palmer, D. M. & BAT Team 2020, GCN Circ., 27665, https://gcn.gsfc.nasa.gov/gcn3/27665.gcn3
Park, G., Koo, B. C., Gibson, S. J., et al. 2013, ApJ, 777, 14
Pavlovic, M. Z., Dobardzic, A., Vukotic, B., & Urosevic, D. 2014, SerAJ, 189, 25
Petroff, E., Hessels, J. W. T., & Lorimer, D. R. 2019, A&ARv, 27, 4
Pinheiro Gonçalves, D., Noriega-Crespo, A., Paladini, R., Martin, P. G., & Carey, S. J. 2011, AJ, 142, 47
Ranasinghe, S., Leahy, D. A., & Tian, W. 2018, OPhyJ, 4, 1
Reid, M. J., Menten, K. M., Brunthaler, A., et al. 2014, ApJ, 783, 130
Ridnaia, A., Golenetskii, S., Aptekar, R., et al. 2020, GCN Circ., 27669, https://gcn.gsfc.nasa.gov/gcn3/27669.gcn3
Shan, W., Yang, J., Shi, S., et al. 2012, ITTST, 2, 593
Sieber, W., & Seiradakis, J. H. 1984, A&A, 130, 257
Surnis, M. P., Joshi, B. C., Maan, Y., et al. 2016, ApJ, 826, 184
Tavani, M., Ursi, A., Verrecchia, F., et al. 2020, ATel, 13686, www.astronomerstelegram.org/?read=13686
The CHIME/FRB Collaboration, Andersen, B. C., Bandura, K. M., et al. 2020, Natur, 587, 54
Vink, J. 2012, A&ARv, 20, 49
Vink, J., & Kuiper, L. 2006, MNRAS, 370, L14
Wang, Y., Beuther, H., Rugel, M. R., et al. 2020, A&A, 634, A83
Wardle, M., & Yusef-Zadeh, F. 2002, Sci, 296, 2350
Wenger, T. V., Balser, D. S., Anderson, L. D., & Bania, T. M. 2018, ApJ, 856, 52
West, J. L., Safi-Harb, S., Jaffe, T., et al. 2016, A&A, 587, A148
Younes, G., Kouveliotou, C., Jaodand, A., et al. 2017, ApJ, 847, 85
Zhang, M. F., Tian, W. W., & Wu, D. 2018, ApJ, 867, 61
Zhong, S. Q., Dai, Z. G., Zhang, H. M., & Deng, C. M. 2020, ApJL, 898, L5
Zhou, P., Safi-Harb, S., Chen, Y., et al. 2014, ApJ, 791, 87
Zhou, P., Vink, J., Safi-Harb, S., & Miceli, M. 2019, A&A, 629, A51
Zhou, X., Yang, J., Fang, M., et al. 2016, ApJ, 833, 4